CrossMark

INVITED FEATURE PAPER

Critical role and modification of surface states in hematite films for enhancing oxygen evolution activity

Myeongwhun Pyeon
Institute of Inorganic Chemistry, University of Cologne, Cologne 50939, Germany

Tero-Petri Ruoko
Laboratory of Chemistry and Biotechnology, Tampere University of Technology, Tampere 33101, Finland

Jennifer Leduc, Yakup Gönüllü, and Meenal Deo
Institute of Inorganic Chemistry, University of Cologne, Cologne 50939, Germany

Nikolai V. Tkachenko
Laboratory of Chemistry and Biotechnology, Tampere University of Technology, Tampere 33101, Finland

Sanjay Mathur[a)]
Institute of Inorganic Chemistry, University of Cologne, Cologne 50939, Germany

(Received 14 September 2017; accepted 29 November 2017)

Hematite films deposited by plasma-enhanced chemical vapor deposition of iron pentacarbonyl [$Fe(CO)_5$] in an oxygen plasma were modified by postdeposition (i) oxygen plasma treatment and (ii) short annealing treatments to reduce the defects and to modify the (sub)surface states and consequently the photoelectrochemical properties. The oxygen plasma treatment resulted in the increase of particle size and augmented surface roughening by densification of grains. Moreover, it induced saturated surface states with reactive oxygen species (O^-, OH^-), evident in the X-ray photoelectron spectroscopy (XPS). Under standard illumination (1.5 AM; 100 mW/cm^2; 150 W xenon lamp), when compared to the pristine hematite coating (0.696 mA/cm^2 at 1.23 V versus RHE and 0.74 V_{onset}) the oxygen plasma-treated films showed severe deterioration in photocurrent density of 0.035 mA/cm^2 and an anodic shift in the onset potential (1.10 V_{onset}) due to oxygen rich surface. In a second set of experiments, the oxygen plasma-treated hematite films were briefly annealed (10 min at 750 °C) and the signals of Fe 2*p* and O 1*s* recovered to higher binding energies, indicating the formation of oxygen vacancies. In addition, a superior photocurrent density value of max. 1.306 mA/cm^2 at 1.23 V versus RHE to that of the pristine hematite photoanode with 0.74 V_{onset} was obtained. Transient absorption spectroscopy further elucidated that the oxygen plasma-induced electron trap states acting as recombination centers that are unfavorable for photoelectrochemical activity. The alteration in Fe:O stoichiometry and thus photocurrent density are corroborated by determination of water oxidation rates in annealed (7.1 s^{-1}) and oxygen plasma treated (2.5 s^{-1}) samples.

I. INTRODUCTION

In the context of alternative energy concepts, an economically viable hydrogen cycle carries the potential for becoming the fuel of the future.[1,2] The conventional hydrogen production relies on the reforming of hydrocarbons obtained from petrochemicals, which makes this technology less environmental friendly due to the significant carbon footprint. Since Fujishima and Honda[3] had demonstrated water photolysis of TiO_2 under UV illumination in 1972, massive attention to the splitting of water into hydrogen and oxygen in a photoelectrochemical (PEC) way has been drawn as a promising alternative route for clean and renewable energy production. Although photoelectrochemical (PEC) water splitting represents a promising avenue for sustainable production of hydrogen, it depends on the availability of suitable photocatalysts with long-term stability and high surface activity in catalyzing the water-splitting reaction. Moreover, they must have certain properties to be useful as photoelectrodes in PEC water splitting, such as appropriate band gap for efficient absorption of solar spectrum, high stability in aqueous electrolytes, and proper positioning of band edges to straddle the water reduction and oxidation potentials. Apart from the electronic boundary conditions (band gap energies and band edge positions), a promising material would need to be robust under photoelectrochemical cycling. Hematite (α-Fe_2O_3) has

Contributing Editor: Xiaobo Chen
[a)]Address all correspondence to this author.
e-mail: sanjay.mathur@uni-koeln.de
This paper has been selected as an Invited Feature Paper.
DOI: 10.1557/jmr.2017.465

https://doi.org/10.1557/jmr.2017.465 Published online by Cambridge University Press

 © Materials Research Society 2018

been investigated in numerous reports[4–7] for application in solar hydrogen production due to its high theoretical solar-to-hydrogen (STH) efficiency of 15%.[8] However, due to its detrimental electronic properties, practical performance of hematite as an efficient photoelectrode is impeded. To overcome the limitations hindering the ideal performance in PEC water splitting, a variety of approaches has been suggested such as elemental doping to boost electrical conductivity, designing heterojunctions for efficient charge carrier separation, nanostructuring for improved light absorption, and these strategies are often combined aiming for the synergetic effect to realize highly efficient photoelectrodes in the PEC splitting of water.[9–12] As a consequence, better understanding of the PEC process using hematite photoelectrodes is achieved; however, the role of surface states on the energetics of the hematite–water interface still remains elusive despite the early dedication to photocatalytic semiconductor surfaces and following numerous elucidations on the hematite surface.[13–15] Wang et al. have shown that the equilibrium potential of hematite anodes depends on the chemical states that can be influenced by surface coatings.[16] Moreover, Durrant et al.[17] and Li et al.[18] demonstrated that surface passivation of hematite photoanodes by coating the substrates with cocatalysts (e.g., Co or Ni hydroxides) can reduce the external electrical bias required for water splitting and retard the surficial electron–hole recombination. Furthermore, application of thin conformal coatings on hematite surfaces was shown to reduce the overpotential, stabilize the electrode–electrolyte interface and passivate surface defects.[19–22]

This work reports on the two-step modification of hematite films deposited by plasma-enhanced chemical vapor deposition (PECVD) of iron pentacarbonyl. To understand the role of surface states and nonstoichiometry in Fe_2O_3 films, the post synthesis treatment of hematite films in oxygen plasma and short-term annealing were investigated. The in-depth investigation on surface structure states via XPS and XAS enabled to verify a chemical transition of the hematite surface that influenced PEC water splitting performance, which was corroborated by charge dynamics analyses via TAS.

II. EXPERIMENTAL

Fe_2O_3 coatings were deposited by the PECVD technique adopting the method previously reported by our group.[23,24] Fluorine-doped tin oxide (F:SnO_2, ~13 Ω/sq, Sigma Aldrich, St. Louis, Missouri) substrates were cleaned by sonicating in Hellmanex III, acetone, and isopropanol for 10 min each. Iron pentacarbonyl [$Fe(CO)_5$, Acros Organics, Geel, Belgium] was introduced simultaneously with 20 sccm (standard cubic centimeters per minute) oxygen used as the reactive plasma gas at the radio frequency (RF, 13.56 MHz) and plasma power of 100 W. Upon completion of the deposition process, the samples were annealed in air at 750 °C (heating rate of 1200 °C/h) for 2 h to obtain a crystalline phase of the Fe_2O_3 layer and the samples were subsequently quenched to room temperature. The high temperature annealing of the as-deposited FeO_x was performed to induce in situ Sn diffusion into the hematite photoanode from the FTO substrates.[25] As post-deposition treatments, these crystalline pristine hematite films were additionally treated in plasma with either oxygen or argon gas (20 sccm; 100 W) for 10, 20, and 30 min in the PECVD chamber. A small part of the FTO was marked to prevent erosion of the back contact from highly reactive charge bombardment during the plasma process. Following the plasma treatment, a short annealing (denoted as SA in figures) was conducted by placing the samples for 10 min in an oven set to 750 °C, and the samples were quenched to ambient conditions.

A three-electrode PEC cell fitted with a saturated calomel electrode (4.5 M KCl, SCE) in 1 M NaOH electrolyte was used to evaluate the PEC performance of the photoelectrodes (area of 0.64 cm^2). Linear scan voltammetry curves were obtained with a potentiostat (Versastat 4, AMETEK, Oak Ridge, Tennessee) using a xenon lamp (AM 1.5 filter, 150 W, Oriel, Irvine, California) as an irradiation source. The voltage scan rate was 10 mV/s. Here the onset potentials were determined by reading the voltage where the photocurrent density reached 0.02 mA/cm^2.[20,26,27] The surface morphology and roughness of the samples were investigated using SEM (Lyra 3-FEG, TESCAN, Brno-Kohoutovice, Czech Republic) and AFM (XE-100, Park Systems, Suwon, South Korea), respectively. The crystallinity of Fe_2O_3 photoanodes was evaluated by a X-ray diffraction system (STOE) with Cu K_α (λ = 1.54184 Å) irradiation. The measured XRD patterns were smoothed with a 20 point Savitzky–Golay filter to remove the unwanted noise. In addition, surface state characterization was conducted using XPS (ESCA M-Probe, Surface Science Instruments, Caltech, Pasadena, California) and the obtained spectra were analyzed by CasaXPS (Casa Software Ltd., Teignmouth, United Kingdom) with charge correction with respect to the C 1*s* peak set at 284.8 eV. Furthermore, in-depth studies on surface chemical states were carried out by X-ray absorption spectroscopy (XAS). The in situ XAS measurements of the O K- and Fe $L_{2,3}$-edges were carried out in total-electron-yield (TEY) mode at BL20A1 at the National Synchrotron Radiation Research Center in Taiwan. The spectra were recorded in the dark and under illumination (1.5 AM solar simulator, HAL-302, Asahi Spectra Co. Ltd., Tokyo, Japan).

The kinetics of photogenerated electrons and holes were studied using flash-photolysis transient absorption spectroscopy in a PEC cell with an Ag/AgCl electrode (3 M NaCl) in 0.1 M NaOH. A Nd:YAG laser (LF117, Solar TII, 10 ns pulse width, 0.33 Hz repetition rate) was

https://doi.org/10.1557/jmr.2017.465 Published online by Cambridge University Press

used to generate third harmonic (F015, Solar TII) 355 nm wave length pulses used as excitation source (attenuated to 0.54 mJ/cm^2). A stabilized halogen lamp (SLS201/M, Thorlabs, 9 W) was used to provide the white light probe beam. The monochromatic (CM110, Digikröm, Spectral Products, Putnam, Connecticut) transient signal was detected with a silicon photoreceiver (2051-FS, New Focus, Santa Clara, California) and recorded on a digitizing oscilloscope (TDS5032B, 350 MHz, Tektronix, Beaverton, Oregon). The transient absorption decays were averaged over 300 laser shots at 575 and 650 nm probe wavelengths, using 50,000 points per decay and 40 μs per point for a total of 2 s decay length. A 100 kHz high-frequency filter was used in the photoreceiver amplifier, joined with a 35 μs RC-filter connected to the oscilloscope to reduce high-frequency noise in the decays. The decays were averaged with a running 10-base logarithmic average to smooth the longer timescale decays.

III. RESULTS AND DISCUSSION

Nanostructured iron oxide films were deposited by plasma-assisted chemical vapor deposition of iron pentacarbonyl [$Fe(CO)_5$] used as source for iron in oxygen plasma to produce homogeneous coatings of amorphous iron oxides. Scanning electron micrographs (Fig. 1) recorded to comparatively analyze the effect of post treatments (oxygen bombardment and rapid annealing treatment) on morphology evolution showed significant changes in the pristine and oxygen plasma-treated films. An iron oxide film synthesized by PECVD exhibits an island structure consisting of ~100 nm sized primary particles agglomerated, which results in a porous structure [see Fig. 1(a)]. When the oxygen plasma is applied on this island structured film, there is remarkable reduction of spacing between agglomerates accompanying particle coarsening. Microscopic analyses showed that the additional oxygen plasma treatment promoted crystallization and growth of hematite particles [Figs. 1(a)–1(d)] possibly driven by the tendency to reduce the grain boundaries. However, upon rapid annealing, no significant change was observed in the morphology, presumably due to the short annealing steps that did not allow any pronounced bulk diffusion and film densification.

Nevertheless, annealing of oxygen plasma-treated samples showed an increased surface roughness and coarsening of grains indicating that the bombardment of oxygen species enhanced the coalescence of smaller particles to form larger ones, whereby the grain growth is controlled by the energetics associated with the grain boundaries, free energy of the interface and the film–substrate interface (see Table I and Fig. 2). The pristine film treated with oxygen plasma for 10 min followed by short annealing shows the highest roughness value of 20.708 nm (R_q, root-mean-square) and 16.390 nm (R_a, average) that gradually decreased with the increasing oxygen plasma exposure time. This surface roughening is attributed to agglomeration of particles induced by easy diffusion of oxygen in the grain boundaries to improve the Fe:O stoichiometry in favor of hematite (Fe_2O_3) as the plasma-CVD grown films are generally oxygen-deficient. In addition, oxygen plasma treatments remove any surface contaminants and change the nature of functional groups into the O-rich surface due to the reactive nature of oxygen species present in the oxygen

TABLE I. Quantified surface roughness of the pristine and the treated hematite films.

Samples	R_{pv} (nm)	R_q (nm)	R_a (nm)
Pristine	72.320	14.323	11.354
10 min O_2-SA	101.768	20.708	16.390
20 min O_2-SA	98.394	19.723	15.296
30 min O_2-SA	91.898	15.939	12.087

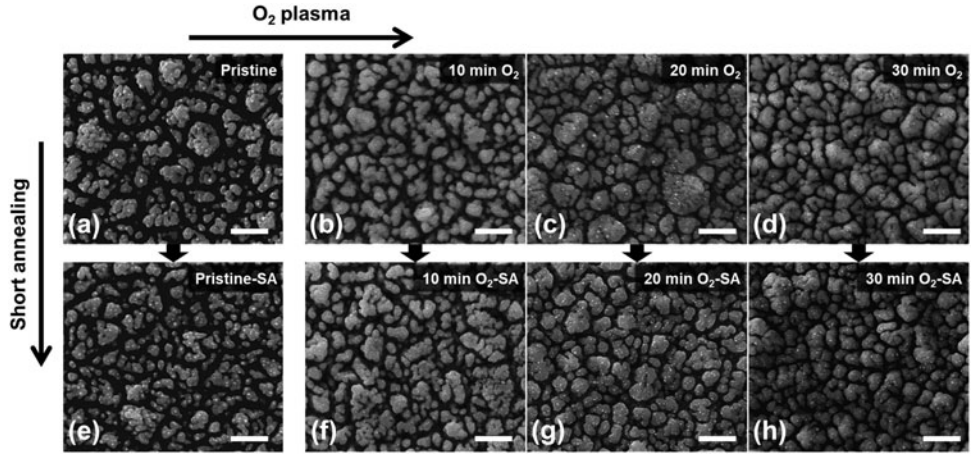


FIG. 1. Upper row: Hematite films treated with oxygen plasma for (a) 0 min, (b) 10 min, (c) 20 min, and (d) 30 min, Lower row: Hematite films that were shortly annealed (at 750 °C for 10 min) on the oxygen plasma-treated samples for (e) 0 min, (f) 10 min, (g) 20 min, and (h) 30 min. Scale bars are 500 nm.

https://doi.org/10.1557/jmr.2017.465 Published online by Cambridge University Press

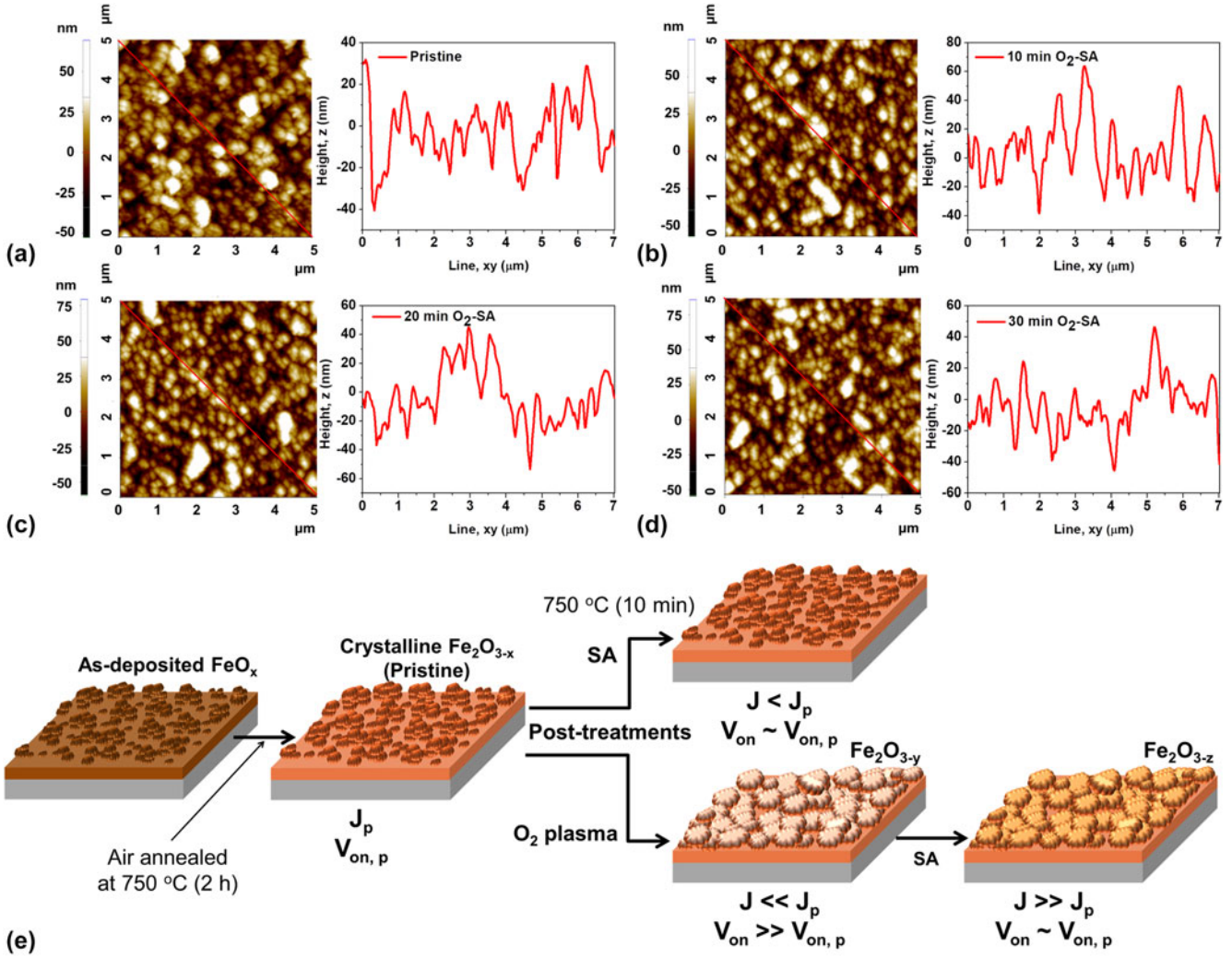


FIG. 2. AFM images and diagonal line profiles of the prepared samples; (a) pristine hematite, oxygen plasma treated for (b) 10 min, (c) 20 min, and (d) 30 min followed by short annealing. (e) Schematic representation of the changes in morphological features as a function of post-synthesis treatments.

plasma. Consequently, the asorbed oxygen species preferentially migrate inwardly upon the heat treatment manifested in the flattening of the surface and abnormal grain growth (Table I).

Evaluation of the crystallographic data provided insight in the crystallization of iron oxide films as a consequence of the post-synthesis treatments. The X-ray diffractogram of the pristine sample exhibited a pure hematite phase (PDF 87-1164) with corresponding diffraction peaks that could be indexed as (012), (104), (110), and (024) planes (Fig. 3). In the oxygen plasma-treated films the signal due to the (024) plane was found to be dimished indicating the influence of oxygen diffusion on crystallographic orientation of the grains. However, all samples exhibited XRD patterns corresponding to the hematite phase without the coexistence of any other iron oxides, which indicates that post treatments procedure did not influence the bulk

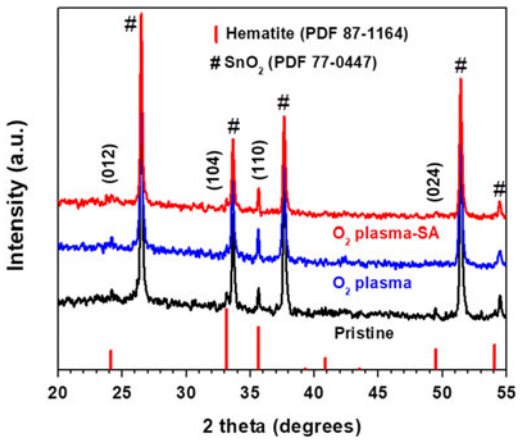


FIG. 3. XRD patterns of the pristine and the post-treated hematite (20 min O_2 plasma followed by the SA) photoanodes.

https://doi.org/10.1557/jmr.2017.465 Published online by Cambridge University Press

crystallinity as evident in the comparable intensities and broadness of the signals (Fig. 3).

The *J–V* curves of the pristine and post-treated hematite photoanodes (Fig. 4) revealed that onset potentials of the hematite photoanodes treated with oxygen plasma exhibited a significant anodic shift. The photoanode treated with oxygen plasma for 10 min exhibited the strongest anodic shift of 360 mV compared to the pristine sample and the lowest photocurrent density of 0.035 mA/cm^2 at 1.23 V versus RHE. However, the following short annealing steps recovered the onset potentials and increased photocurrent density when compared to the pristine hematite photoanode. For instance, the highest photocurrent density of 1.306 mA/cm^2 at 1.23 V versus RHE was obtained from the sample treated with oxygen plasma for 20 min followed by short annealing [see Fig. 4(b)]. Moreover, *J–V* curves of the pristine hematite photoanode and the short-annealed hematite without preceding oxygen plasma treatment are comparable [Fig. 4(c)]; the photocurrent density of the short-annealed sample was lower in the whole range of applied potentials, and its onset potential was almost the same as that of the pristine photoanode. This observation suggested that the oxygen plasma treatment prior to rapid annealing is crucial to fabricate efficient hematite photoanodes. The values of onset potential and the photocurrent density at 1.23 V versus RHE are listed and depicted in the insets of Fig. 4 and in Fig. 4(d), respectively.

As pointed out by Grätzel et al.[28] and other related reports, the onset potential of hematite photoanode can be improved by chemical surface modification.[29–31] We observed that the physical treatment of hematite films in oxygen plasma changed the surface states and chemical environment around Fe centers that was supported by XPS studies. The Fe 2*p* spectrum (Fig. 5) of pristine hematite showed two distinct peaks, Fe $2p_{3/2}$ at 710.95 eV and Fe $2p_{1/2}$ at 724.40 eV with a shakeup satellite located at 718.65 eV, which is a typical feature of Fe_2O_3.[32,33] After the oxygen plasma treatment, the

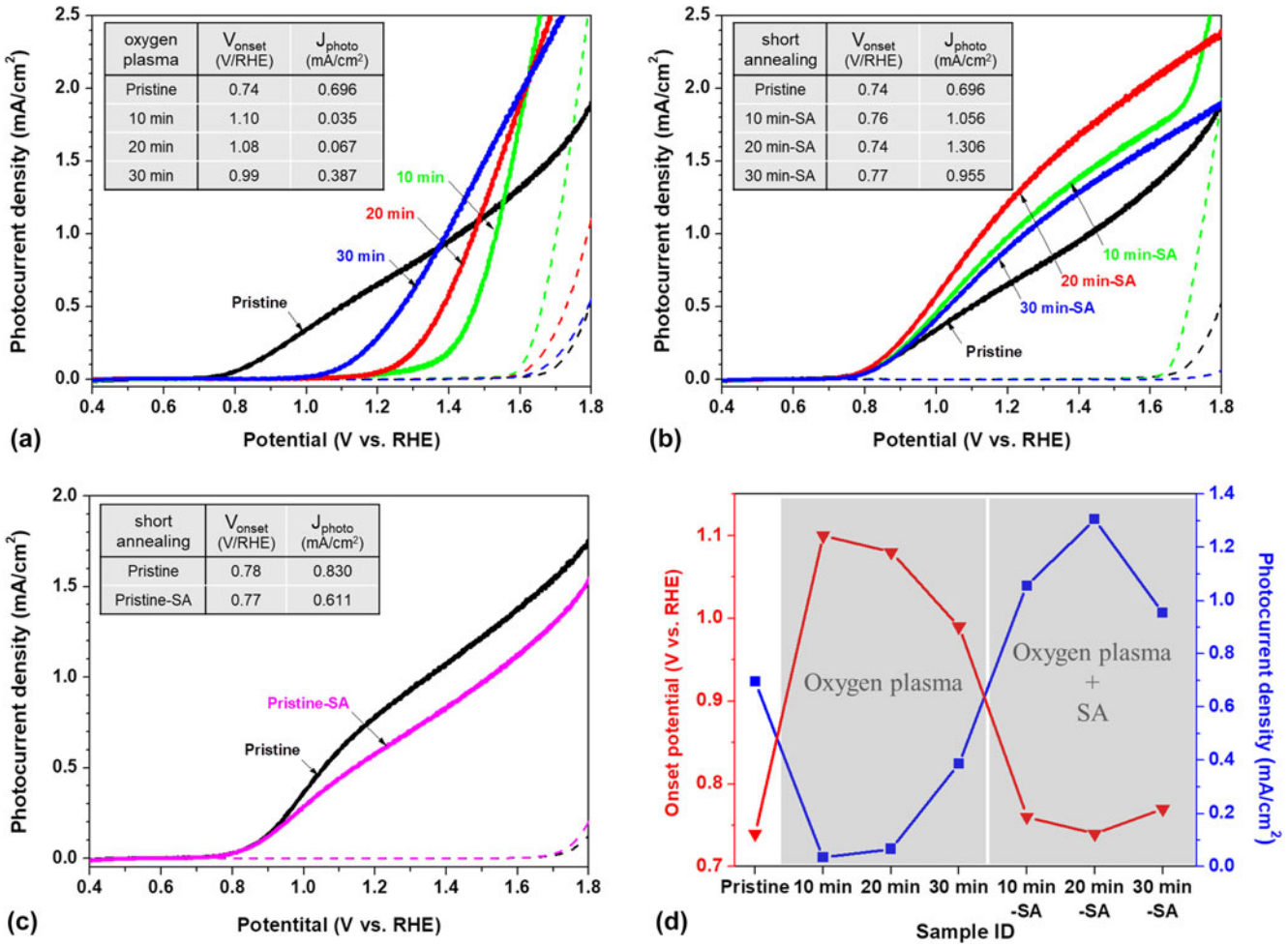


FIG. 4. *J–V* curves of the prepared hematite photoanodes (a) only treated with O_2 plasma, (b) treated with the oxygen plasma followed by short annealing (SA); (c) comparison between a pristine and short-annealed samples and (d) a graphical demonstration of onset potential and photocurrent density change at 1.23 V versus RHE based on insets in (a) and (b).

https://doi.org/10.1557/jmr.2017.465 Published online by Cambridge University Press

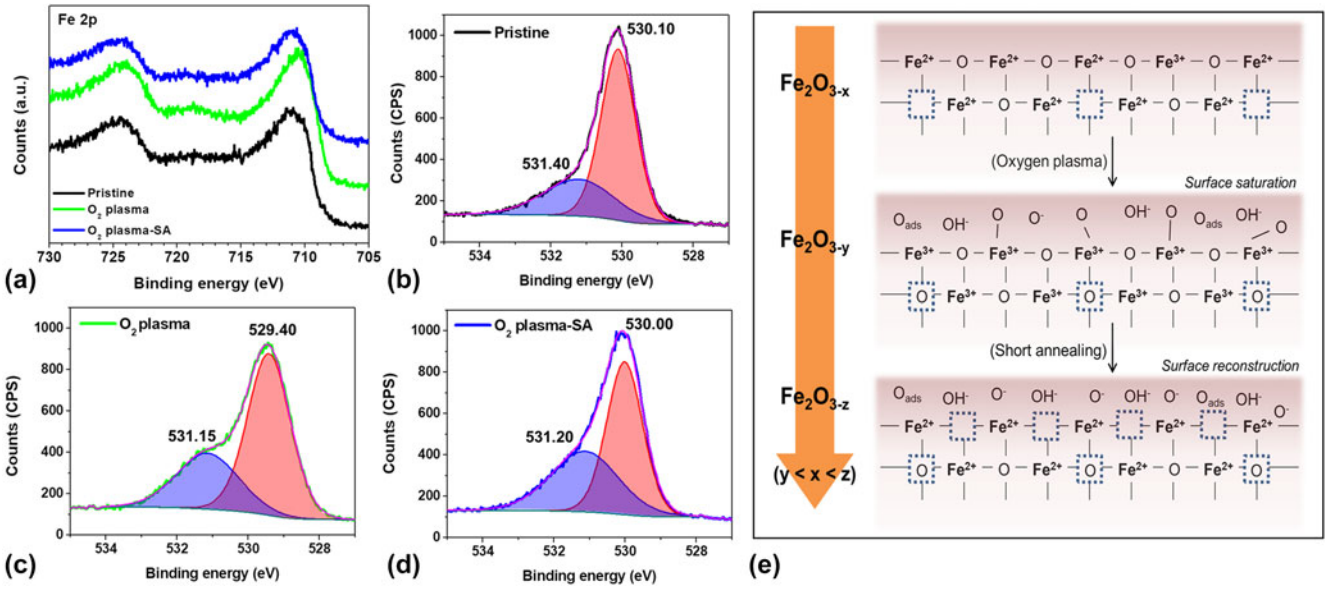


FIG. 5. Comparisons of XPS spectra between the pristine and the post-treated hematite (20 min O_2 plasma followed by the SA); (a) spectra of Fe 2*p* peaks, (b, c, and d) spectra of O 1*s* peaks of the pristine, O_2 plasma treated and O_2 plasma followed by SA treated samples, respectively, and (e) a proposed scheme of hematite surface upon the post-treatments.

shakeup satellite peak which represents the oxidation state of Fe^{3+} became stronger indicating higher compositional uniformity.[33] The XPS studies suggested that the surface of the pristine hematite is intrinsically oxygen deficient (Fe_2O_{3-x}) and the oxygen plasma saturates the surface defects via preferential adsorption of oxygen species. Moreover, the signals of Fe $2p_{1/2}$ (724.40 eV) and Fe $2p_{3/2}$ (710.95 eV) in the pristine sample showed a shift toward lower binding energies (724.05 and 710.15 eV) possibly due to additional electronic charges and changed chemical environment around Fe centers, which presumably resulted in higher shielding of core electrons. After further short annealing step, the binding energies of the Fe 2*p* core levels recovered to 724.30 eV (Fe $2p_{1/2}$) and 710.65 eV (Fe $2p_{3/2}$), which is often the evidence for formation of oxygen vacancies.[34] A similar trend in binding energy shift was observed in the O 1*s* peak at ~530 eV (Fe–O), along with a shoulder peak at ~531 eV generally accepted as a contribution of surface adsorbed oxygen species (e.g., O_{ads}, O^-, OH^-).[35] These surface oxygen species were still evident after the short annealing step, while the main O 1*s* peak was found to shift back to a higher binding energy. Furthermore, the shift in O 1*s* peak from 530.10 to 529.45 eV upon oxygen plasma treatment is in good agreement with a previously reported value for lattice oxygen (O^{2-}).[36] The peak area of the O 1*s* signals at ~530 eV significantly increased after the oxygen plasma treatment (from 965.0 to 1194.4), confirming an increased amount of surface-attached Fe–O groups, whereas it decreases upon the short annealing from 1194.4 to 896, indicating either the loss of oxygen or inward migration of oxygen [Fig. 5(e)].

We presume that the hematite surface (Fe_2O_{3-x}) that is intrinsically oxygen deficient becomes saturated with an excess of oxygen species (O_{ads}, O^-, OH^-) upon oxygen plasma treatment, leading to an increased concentration of Fe^{3+} species [Fig. 5(a)] and an increased area of the shoulder peak at ~531 eV [compare Figs. 5(b) and 5(c)]. This oxygen-saturated surface with filled up oxygen vacancies impedes water oxidation by reducing surface occupancy of iron centers that was revealed as a faster water oxidation route than oxygen surface states.[36] During the thermal treatment, the saturated hematite surface with an excess amount of oxygen species can be reconstructed, inducing an optimized amount of oxygen vacancies for an efficient oxygen evolution reaction (OER).[37] It corresponds to the earlier studies dealing with the role of oxygen vacancies[34–37] and oxygen deficient hematite as reported by Cowan et al.[38] Based on the surface analyses, we propose the surface stoichiometry of crystalline hematite as Fe_2O_{3-x} for the pristine samples, Fe_2O_{3-y} for the oxygen plasma treated, and Fe_2O_{3-z} for the oxygen plasma followed by short annealing sample, where $y < x < z$.

To verify the proposed oxygen-deficient surface structure of pristine hematite and to investigate the transfer direction of photogenerated electrons upon illumination with monochromatic incident light, (in situ) X-ray absorption spectroscopy (XAS) was performed. In contrast to XPS, XAS probes unoccupied states using soft X-ray synchrotron radiation (<5000 eV). Thereby, core electrons of an atom absorb X-ray photons and get promoted to higher-lying unoccupied states forming short-lived excited states. Moreover, K-edge XAS is an

https://doi.org/10.1557/jmr.2017.465 Published online by Cambridge University Press

effective tool to approximate the electronic and structural properties affecting OER catalysis.[39] In hematite, the electronic transitions from O 1*s* to hybridized O 2*p*-Fe 3*d* states and from Fe 2*p* to Fe 3*d* states can be verified by the O K-edge (photon energies of 520–570 eV) and the Fe $L_{2,3}$-edge (700–730 eV) spectra, respectively. Since the intensity of the signals in the XAS is directly proportional to the amount of unoccupied states, changes in the electronic structure triggered, e.g., by doping or the formation of composite materials can be unambiguously detected.[40,41] Fu et al., for instance, showed that Ta-doping of α-Fe_2O_3 nanorods films did not affect the Fe 3*d* but the O 2*p* site. Upon doping, the signal corresponding to the O 2*p*-Fe 3*d* t_{2g} state decreased in intensity which implies that electrons get transferred to this oxygen site. This has been reported to lower the conduction band and thus to enhance the electron conductivity.[42] As XAS exhibits very high sensitivity toward the chemical environment of an atom, this method was used herein as a sensitive local structure probe to clarify the surface structure of the pristine hematite sample. Both the Fe L-edge and O K-edge spectra were recorded in surface sensitive total electron yield. The oxidation state of iron in pristine hematite films was first investigated by Fe L-edge spectra [Fig. 6(b)]. Due to Fe 2*p* spin–orbit coupling the spectra are divided into 2 parts, the Fe L_3 and L_2 edges, located at ~710 and ~723 eV, which have been assigned to Fe $2p_{3/2}$ and Fe $2p_{1/2}$ transitions to an unoccupied 3*d* orbital, respectively.[43] Both of these edges are further split into two peaks with intensity ratios that are sensitive toward the oxidation state of iron, resulting from an interplay of the crystal field and electronic interactions.[43,44] In a simplified model, the splitting was solely ascribed to crystal field interactions with the signals at the L_3 edge corresponding to t_{2g} and e_g states. As displayed in Fig. 6(b), the e_g states exhibit a higher intensity than the t_{2g} states. This is in agreement with literature reported spectra for α-Fe_2O_3.[40,42] In contrast, the L_3 edge of Fe^{2+} shows a reversed intensity ratio with the main peak located at ~707 eV and a shoulder toward higher energy (~709 eV).[45] The oxygen K-edge spectrum [Fig. 6(a)] shows four distinct components at around 528, 539, 547, and 560 eV. As a result of the crystal field effect, the signal at around 527–532 eV is further split into two peaks of equal intensity corresponding to the lower energy 3*d* t_{2g} and higher energy 3*d* e_g states reflecting the octahedral environment of Fe^{3+} in α-Fe_2O_3.[42,46] The broad absorption feature at around 532–544 eV is attributed to O 2*p*-Fe (4*s*, 4*p*) hybridized states, and the high energy structure at about 550–570 eV has been reported to result from resonance scattering.[41,47] The signal at 545–549 eV, however, shows a higher intensity than reported for α-Fe_2O_3.[47] This has been likewise reported for α-Fe_2O_3 single crystals, which were first subjected to a reductive treatment under ultra-high vacuum at 950 °C and afterward reoxidized via an additional heating step under a fixed oxygen pressure of 10^{-6} mbar for 90 min.[46,47] Thus, this feature could derive from the oxygen deficient Fe_2O_{3-x} surface as a result of the distortion of octahedra by oxygen vacancies. However, the origin of the change in the fine structure of the XAS spectrum requires further investigation. It was reported that the intensity ratio of the O 2*p*-Fe 3*d* signal relative to the broad O 2*p*-Fe (4*s*, 4*p*) signal directly reflects the extent of covalent bonding in α-Fe_2O_3 and that an increased O 2*p*-Fe 3*d* hybridization results in accelerated surface oxidation reaction kinetics.[41] Thus, along with the results gained from XPS analysis and PEC measurements, oxygen plasma treatment reduced the degree of O 2*p*-Fe 3*d* hybridization resulting in an anodic shift of the onset potential.

In case of in situ XAS the sample is additionally illuminated by monochromatic incident light (350–750 nm) which permits to elucidate which orbitals are photocatalytically active as well as the transfer of photogenerated electrons in composite materials. Herein, both the spectra at the Fe L-edge and the O K-edge were recorded in the dark (black graphs) and under illumination (blue, red graphs). The insets in Fig. 6 show the enlarged spectra in (a) the O 2*p*-Fe 3*d* and (b) the

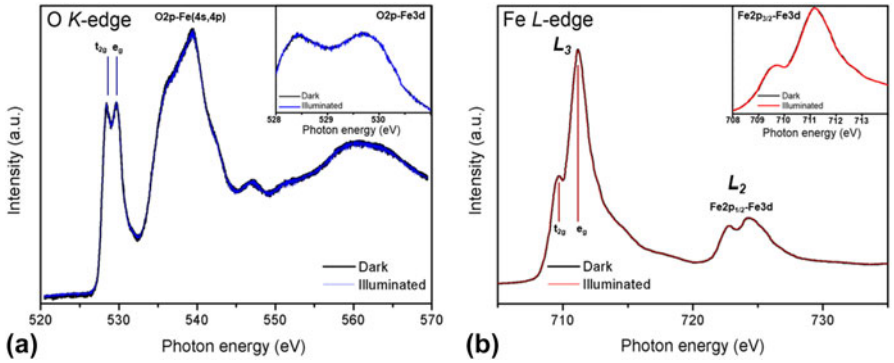


FIG. 6. In situ XAS measurements of pristine hematite (a) at the oxygen K-edge and (b) at the iron L-edge measured in the dark and under illuminated conditions. The insets show the enlarged spectra in (a) the O 2*p*-Fe 3*d* and (b) the Fe $2p_{3/2}$-Fe 3*d* region.

https://doi.org/10.1557/jmr.2017.465 Published online by Cambridge University Press

Fe $2p_{3/2}$-Fe 3*d* region. No spectral differences (both at the O K-edge and the Fe L-edge) were observed in the dark and under light illumination. This can be ascribed to a rapid electron–hole recombination as a result of the intrinsically oxygen-deficient Fe_2O_{3-x} structure.

Submillisecond to second timescale TAS analysis was used to elaborate the charge carrier dynamics in detail and to further corroborate PEC performances influenced by surface chemical states of the hematite photoelectrodes. The transient absorption spectrum of hematite in this timescale is composed of two distinct spectral features. The most pronounced spectral feature is a narrow negative transient absorption band (bleach) centered at 570–580 nm that forms in the nanosecond to microsecond timescale,[48] which was observed originally by Durrant et al.,[49,50] later by Lemmetyinen et al.,[48] and assigned to electron trapping into localized energy states near the conduction band edge with a lifetime in the millisecond timescale. The second spectral feature is a broad positive absorption band peaking at 650 nm that has a lifetime in the hundreds of milliseconds timescale.[48] This feature is only visible under anodic bias and the transient absorption amplitude of the feature correlates extremely well with the photocurrent density of the photoanode.[49,51] Since the lifetime of this feature is reduced drastically when hole scavengers are added to the electrolyte, it is reasonable to assign the feature to long-lived photogenerated holes in the depletion region.[39,48] The transient absorption decays at 575 and 650 nm of pristine, 20 min oxygen plasma-treated, and 20 min oxygen plasma-treated and short-annealed samples under 1.50 V versus RHE bias voltage are presented in Fig. 7 along with the respective biphasic fits. The absorption spectra (Fig. S2) and transient absorption decays at bias voltages of 0.90 and 1.23 V versus RHE (Figs. S3 and S4) along with the complete fit results (Tables II and III) can be found in the Supplementary Material.

The function used for fitting the TAS decays herein is of the form $\Delta A = A_1 \exp\left[(-t/\tau_1)^{\beta_1}\right] + A_2 \exp\left[(-t/\tau_2)^{\beta_2}\right]$, where A_i are the amplitudes, τ_i are the lifetimes, and β_i are the stretching factors of the stretched exponential decay components. The stretched exponential function is now used to describe relaxation in a disordered system, and both the lifetimes and stretching factors are reported in Table II. The stretching factor was limited to values between 0 and 1, with 1 giving the usual exponential function. The obtained lifetimes and stretching factors were used to calculate the mean lifetimes using $\tau_i = \frac{\tau_i}{\beta_i}\Gamma\left(\frac{1}{\beta_i}\right)$, where τ_i is the mean lifetime and Γ is the gamma function. The mean lifetimes are presented in

TABLE II. Stretched exponential lifetimes and the associated stretching factors obtained from the biphasic fits to raw data.

Samples	Bias voltages (V)	τ_i (ms)	β_1	τ_2 (ms)	β_2
Pristine	0.90	0.44 ± 0.86	0.36 ± 0.20	215 ± 86	0.76 ± 0.33
	1.23	1.90 ± 0.84	1.00 ± 0.23	432 ± 79	0.85 ± 0.19
	1.50	2.30 ± 0.58	1.00 ± 0.01	447 ± 64	0.79 ± 0.13
O_2 plasma	0.90	0.17 ± 0.34	0.32 ± 0.19	14 ± 14	0.31 ± 0.07
	1.23	0.17 ± 0.08	0.44 ± 0.07	68 ± 17	0.49 ± 0.07
	1.50	0.12 ± 0.03	0.44 ± 0.03	322 ± 32	0.74 ± 0.08
O_2 plasma-SA	0.90	0.07 ± 0.38	0.36 ± 0.42	12 ± 13	0.28 ± 0.06
	1.23	0.22 ± 0.28	0.47 ± 0.18	173 ± 45	0.72 ± 0.21
	1.50	0.61 ± 0.32	0.75 ± 0.25	83 ± 21	0.55 ± 0.11

TABLE III. Mean lifetimes calculated from the lifetimes and stretching factors along with the raw and relative amplitudes of the decay components at 650 nm from the fits.

Samples	Bias voltages (V)	$\langle\tau_1\rangle$ (ms)	A_1 (μOD)	$\langle\tau_2\rangle$ (ms)	A_2 (μOD)	A_1 (%)	A_2 (%)
Pristine	0.90	2.0	48	250	16	75	25
	1.23	1.9	16	470	33	32	68
	1.50	23	11	510	45	19	81
O_2 plasma	0.90	1.2	71	110	47	60	40
	1.23	0.4	80	140	70	53	47
	1.50	03	74	390	81	48	52
O_2 plasma-SA	0.90	0.3	41	150	35	54	46
	1.23	0.5	55	210	32	63	37
	1.50	0.7	20	140	48	29	71

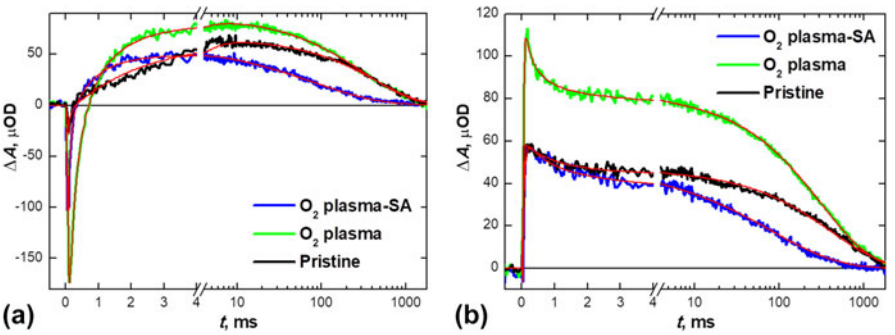


FIG. 7. Transient absorption decays of the samples under 1.50 V versus RHE bias, (a) at 575 nm and (b) at 650 nm.

https://doi.org/10.1557/jmr.2017.465 Published online by Cambridge University Press

Table III along with the absolute and relative amplitudes of the decay components at 650 nm.

The most noticeable feature of the decays is that the transient absorption amplitude at 100 μs increases almost 7-fold at 575 nm (-2.6×10 μOD for pristine versus -1.73×10^2 μOD for O_2 plasma) and 2-fold at 650 nm (5.9×10 μOD for pristine versus 1.13×10^2 μOD for O_2 plasma) after 20 min of oxygen plasma treatment (see Fig. 7). This is a striking difference when taking into account that the same excitation density was used for all samples and the absorption of the pristine sample is the highest at the excitation wave length (Fig. S2). After the short annealing, the transient absorption amplitude at 575 nm recovers slightly to 4-fold that of the pristine sample (-1.03×10^2 μOD), whereas the amplitude at 650 nm recovers completely to the same level of the pristine sample (5.7×10 μOD). The increased transient absorption amplitude at 575 nm indicates a greatly increased amount of electron trap states after the oxygen plasma treatment, whereas at 650 nm the increase in amplitude suggests an increase in the yield of long-lived photoholes.[39] The smaller amplitude of the bleach and the full recovery of the photohole yield for the short-annealed sample indicate a greatly reduced number of electron trap states when compared with the oxygen plasma sample.

The electron traps are presumed to originate from the plasma treatment of the surface, possibly by generation of oxygen vacancies or the formation of trapping oxygen states on the surface of the photoanode. Furthermore, increased electron trapping has been suggested to be a pathway that competes with recombination,[48,50] thus explaining the increased photohole density as probed at 650 nm. The bleach signal is clearly visible for the oxygen plasma-treated sample even at 0.90 V versus RHE (Fig. S3), 0.18 V below the photocurrent onset voltage, suggesting that the increased electron trapping is due to newly formed surface states instead of the previously reported intraband trap states within the depletion region. These trap states seem to also act as efficient recombination centers, as indicated by the fast recombination component of the photoholes, being much more pronounced for the oxygen plasma-treated sample (see Table II). The increased amount of recombination centers explains the drastically higher photocurrent onset voltage of the oxygen plasma treated sample, whereas the onset voltage is the same for the pristine and short-annealed samples [see Fig. 4(c)]. This indicates that even though the newly formed electron trap states suppress the sub-microsecond recombination, the millisecond timescale recombination with surface photoholes is increased. This negatively affects the OER, leading to an increased photocurrent onset voltage.

At 1.50 V versus RHE the water oxidation reaction dominates the long-lived decay of the photohole signal at both 575 and 650 nm. Both pristine and oxygen plasma-treated samples have approximately the same water oxidation rate of 2.0–2.5 s^{-1} (mean lifetimes 510 and 390 ms for pristine and O_2 plasma samples, respectively, see Table II). The long-lived hole decay at 1.23 V remains unchanged for the pristine sample (mean lifetime 470 ms), whereas the lifetime is three times lower for the oxygen plasma-treated sample (mean lifetime 140 ms). The drastic drop in the long-lived hole lifetime is due to the increased back electron hole recombination, indicating that the electron trap states formed by the oxygen plasma treatment also increase long-lived recombination in addition to increasing the millisecond timescale recombination. However, the water oxidation rate of 7.1 s^{-1} for the short-annealed sample is in the faster end of the rates previously reported for hematite photoanodes (mean lifetime 140 ms).[39,48] Since the yield of long-lived holes for the short-annealed sample is approximately the same as for the pristine sample (48 and 45 μOD, respectively), the much faster water oxidation dynamics indicates increased the catalytic activity after oxygen plasma treatment and short annealing. Interestingly, the long-lived hole lifetime remains approximately the same at 1.23 and 0.90 V (see Table II) with only the amplitude of the long-lived component being lower. This indicates that the increased catalytic activity of the photoanode treated with oxygen plasma followed by short annealing is due to a reduced amount of back electron recombination at all measured bias voltages, supporting enhanced PEC performance.

We have additionally conducted investigations on the effect of argon (Ar) plasma onto the PEC activity in comparison to the oxygen plasma treated samples. Figure 8 shows *J*–*V* curves of hematite photoanodes post-treated with Ar plasma and followed by short annealing. Significant anodic shifts of onset potentials were observed for the Ar plasma-treated samples (green curves), which recovered upon further short annealing regardless of the duration of the plasma treatment, which was already observed in Fig. 4. It seems that the anodic shift of the onset potential resulted from plasma bombardment regardless of the type of plasma forming gas. It is surprising that the chemical states at the hematite surface do not seem to be affected by the Ar plasma. High resolution XPS spectra of the Fe 2*p* states given in Fig. S5 support this speculation as there is no evolution of a shakeup satellite peak at ~718 eV, which proves the non-oxidizing nature of Ar plasma in contrast to the oxidizing nature of oxygen plasma. Thus, the chemical states at the hematite surface are highly dependent on the type of plasma. The increased amount of electron trapping states upon oxygen plasma treatment detected at 575 nm [see Fig. 7(a)] is ascribed to surface defects induced by a physically disturbed surface that can be efficient recombination sites. However, the mechanism of anodic shift in the onset potential observed upon Ar plasma needs to be further investigated carefully since chemical reduction of surface yielding recombination

https://doi.org/10.1557/jmr.2017.465 Published online by Cambridge University Press

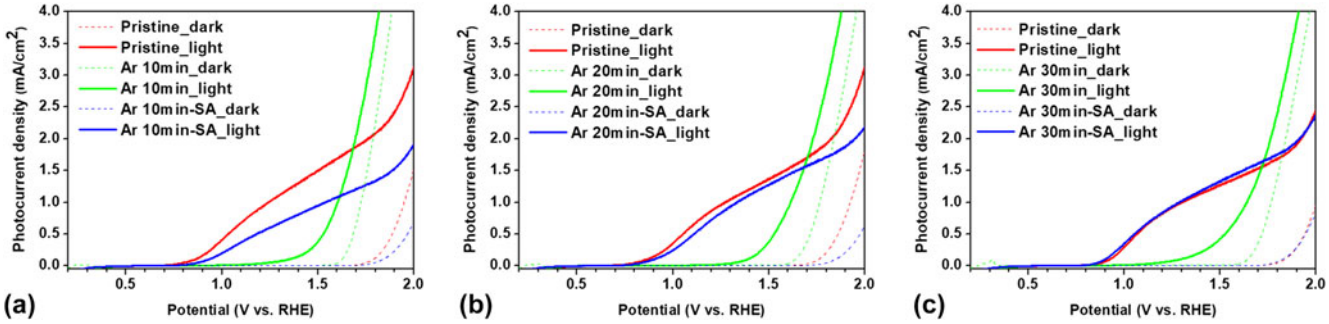


FIG. 8. *J–V* curves of (blue) the pristine hematite, (green) treated only with the Ar plasma, and (blue) treated with the Ar plasma followed by the SA; The Ar plasma for (a) 10 min, (b) 20 min, and (c) 30 min.

centers such as interstitial Fe ions could occur, resulting in anodic onset shift. In addition, the recovery of the onset potential upon further short annealing indicates that the defective surface structure becomes relaxed or reconstructed by the thermal treatment. However, in case of Ar plasma treatment, no superior PEC performance is observed upon the short annealing step. This implies that the intentionally saturated surface with oxygen species contributes critically to the enhancement in PEC performance of hematite. Further investigations on the hematite surface were carried out by water contact angle (WCA) measurements on prepared films. It is well known that the surface oxygen provides hydrophilicity to various surfaces.[52] In the WCA measurement, the pristine hematite film exhibited an average WCA of ~25°, whereas a complete wetting (0°) of the water droplet occurred on the oxygen plasma treated hematite surface. After the additional short annealing step, the WCA value was determined to be ~20°. These results strongly evidence the incorporation of surface oxygen species upon oxygen plasma treatment and the removal of these species upon the short annealing step. On the other hand, the WCA of the Ar plasma treated sample was ~17°, which is slightly lower than the WCA value of pristine hematite. However, after short annealing, the hematite surface showed complete wetting, which was likewise observed for the oxygen plasma treated film. It is likely either due to decreased amount of carbon contents on the surface upon Ar plasma treatment (from 41.20 to 30.74 at.%) or due to roughened surface, resulted from plasma etching and then, atmospheric oxygen species adsorbed during the short annealing would induce hydrophilic nature.[53] To gain a deeper insight on the activation energy needed for oxygen incorporation at surface and subsurface levels, future studies will deal with the modeling of oxygen deficient hematite systems for PEC water splitting.

IV. CONCLUSION

As-grown hematite films by plasma CVD of an iron precursor are generally non-stoichiometric and contain oxygen deficiencies present at both the surface and subsurface levels. The uptake of oxygen upon exposure of pristine hematite films to oxygen plasma followed by short annealing steps show that oxygen incorporation faces an activation barrier. Whereas oxygen plasma leads to a high concentration of surface-attached oxygen species, the annealing of these samples results in concomitant inward migration of chemisorbed oxygen species and desorption of adsorbed oxygen species. Enrichment of oxygen species on the surface reduced the overall PEC performance of the cell, while an enhanced photocurrent was observed in annealed samples due to high concentration of Fe centers on the surface. Although the used post-treatments do not remarkably influence bulk crystallinity or surface morphology of hematite films, it is evident that posttreatments modified the surface states in both cases as manifested in the shifts observed in Fe 2*p* and O 1*s* binding energies. The charge carrier dynamics revealed that the oxygen plasma exposed surface possesses more recombination centers, whereas the electronic trap sites were reduced in annealed samples attributed to surface reconstruction processes as supported by XPS data and a cathodic shift in the onset potential. The improved PEC performance after the post-treatments of hematite photoelectrodes is ascribed to increased catalytic activity as proven by faster water oxidation rate of 7.1 s^{-1} compared to the pristine and the oxygen plasma treated samples (2.0–2.5 s^{-1}). The two surface modification strategies are intrinsically different as the surface treatment in oxygen plasma is subject to the kinetic energies of the impinging oxygen species and therefore somewhat mild when compared to the short annealing treatment at 750 °C that can induce oxygen diffusion through the bulk at subsurface and intergranular level. This interplay of kinetic and thermodynamic factors offers a new playground to design new surface modification strategies in nanostructured films.

ACKNOWLEDGMENTS

The financial support in the framework of the DFG priority program (SPP 1613; "Fuels Produced

https://doi.org/10.1557/jmr.2017.465 Published online by Cambridge University Press

Regeneratively Through Light-Driven Water Splitting: Clarification of the Elemental Processes Involved and Prospects for Implementation in Technological Concepts") and by the University of Cologne is gratefully acknowledged. The authors S.M. and S.H.C. acknowledged a strategic collaboration between the Christiansen research group at Helmholtz-Zentrum Berlin für Materialien und Energie and the AG Mathur. All authors gratefully acknowledge Prof. Dr. Chung-Li Dong from Tamkang University, Tamsui, Taiwan for performing (in situ) XAS and for helpful discussions. The authors T-P.R. and Prof. Nikolai V. Tkachenko contributed to this investigation by conducting TAS analyses. Dr. Meenal Deo would like to acknowledge financial support from Science and Technology Research Board (SERB, India) under Overseas Postdoc Fellowship. Dr. Andreas Mettenbörger and Dr. Alexander Sasinska are acknowledged for helpful discussions.

REFERENCES

1. A. Ursua, L.M. Gandia, and P. Sanchis: Hydrogen production from water electrolysis: Current status and future trends. *Proc. IEEE* **100**, 410 (2012).
2. C. Xiang, K.M. Papadantonakis, and N.S. Lewis: Principles and implementations of electrolysis systems for water splitting. *Mater. Horiz.* **3**, 169 (2016).
3. A. Fujishima and K. Honda: Electrochemical photolysis of water at a semiconductor electrode. *Nature* **238**, 37 (1972).
4. D.A. Grave, H. Dotan, Y. Levy, Y. Piekner, B. Scherrer, K.D. Malviya, and A. Rothschild: Heteroepitaxial hematite photoanodes as a model system for solar water splitting. *J. Mater. Chem. A* **4**, 3052 (2016).
5. K.D. Malviya, H. Dotan, D. Shlenkevich, A. Tsyganok, H. Mor, and A. Rothschild: Systematic comparison of different dopants in thin film hematite (α-Fe_2O_3) photoanodes for solar water splitting. *J. Mater. Chem. A* **4**, 3091 (2016).
6. L. Wang, Y. Yang, Y. Zhang, Q. Rui, B. Zhang, Z. Shen, and Y. Bi: One-dimensional hematite photoanodes with spatially separated Pt and FeOOH nanolayers for efficient solar water splitting. *J. Mater. Chem. A* **5**, 17056 (2017).
7. P. Dias, L. Andrade, and A. Mendes: Hematite-based photoelectrode for solar water splitting with very high photovoltage. *Nano Energy* **38**, 218 (2017).
8. A.G. Tamirat, J. Rick, A.A. Dubale, W-N. Su, and B-J. Hwang: Using hematite for photoelectrochemical water splitting: A review of current progress and challenges. *Nanoscale Horiz.* **1**, 243 (2016).
9. J.A. Glasscock, P.R.F. Barnes, I.C. Plumb, and N. Savvides: Enhancement of photoelectrochemical hydrogen production from hematite thin films by the introduction of Ti and Si. *J. Phys. Chem. C* **111**, 16477 (2007).
10. A. Kleiman-Shwarsctein, Y-S. Hu, A.J. Forman, G.D. Stucky, and E.W. McFarland: Electrodeposition of α-Fe_2O_3 doped with Mo or Cr as photoanodes for photocatalytic water splitting. *J. Phys. Chem. C* **112**, 15900 (2008).
11. W-H. Hung, T-M. Chien, and C-M. Tseng: Enhanced photocatalytic water splitting by plasmonic TiO_2–Fe_2O_3 cocatalyst under visible light irradiation. *J. Phys. Chem. C* **118**, 12676 (2014).
12. S.C. Warren, K. Voitchovsky, H. Dotan, C.M. Leroy, M. Cornuz, F. Stellacci, C. Hebert, A. Rothschild, and M. Gratzel: Identifying champion nanostructures for solar water-splitting. *Nat. Mater.* **12**, 842 (2013).
13. Y. Lin, G. Yuan, S. Sheehan, S. Zhou, and D. Wang: Hematite-based solar water splitting: Challenges and opportunities. *Energy Environ. Sci.* **4**, 4862 (2011).
14. L.M. Peter, K.G.U. Wijayantha, and A.A. Tahir: Kinetics of light-driven oxygen evolution at α-Fe_2O_3 electrodes. *Faraday Discuss.* **155**, 309 (2012).
15. A.J. Bard, F-R.F. Fan, A.S. Gioda, G. Nagasubramanian, and H.S. White: On the role of surface states in semiconductor electrode photoelectrochemical cells. *Faraday Discuss. Chem. Soc.* **70**, 19 (1980).
16. C. Du, M. Zhang, J-W. Jang, Y. Liu, G-Y. Liu, and D. Wang: Observation and alteration of surface states of hematite photoelectrodes. *J. Phys. Chem. C* **118**, 17054 (2014).
17. M. Barroso, C.A. Mesa, S.R. Pendlebury, A.J. Cowan, T. Hisatomi, K. Sivula, M. Grätzel, D.R. Klug, and J.R. Durrant: Dynamics of photogenerated holes in surface modified α-Fe_2O_3 photoanodes for solar water splitting. *Proc. Natl. Acad. Sci. U. S. A.* **109**, 15640 (2012).
18. Y. Yang, M. Forster, Y. Ling, G. Wang, T. Zhai, Y. Tong, A.J. Cowan, and Y. Li: Acid treatment enables suppression of electron-hole recombination in hematite for photoelectrochemical water splitting. *Angew. Chem., Int. Ed.* **55**, 3403 (2016).
19. Y. Liu, X. Yan, Z. Kang, Y. Li, Y. Shen, Y. Sun, L. Wang, and Y. Zhang: Synergistic effect of surface plasmonic particles and surface passivation layer on ZnO nanorods array for improved photoelectrochemical water splitting. *Sci. Rep.* **6**, 29907 (2016).
20. F. Le Formal, N. Tetreault, M. Cornuz, T. Moehl, M. Gratzel, and K. Sivula: Passivating surface states on water splitting hematite photoanodes with alumina overlayers. *Chem. Sci.* **2**, 737 (2011).
21. Y. Yang, R. Xie, Y. Liu, J. Li, and W. Li: Effect of surface passivation on photoelectrochemical water splitting performance of WO_3 vertical plate-like films. *Catalysts* **5**, 2024 (2015).
22. Q. Gui, Z. Xu, H. Zhang, C. Cheng, X. Zhu, M. Yin, Y. Song, L. Lu, X. Chen, and D. Li: Enhanced photoelectrochemical water splitting performance of anodic TiO_2 nanotube arrays by surface passivation. *ACS Appl. Mater. Interfaces* **6**, 17053 (2014).
23. A.P. Singh, A. Mettenbörger, P. Golus, and S. Mathur: Photoelectrochemical properties of hematite films grown by plasma enhanced chemical vapor deposition. *Int. J. Hydrogen Energy* **37**, 13983 (2012).
24. M. Wang, M. Pyeon, Y. Gonullu, A. Kaouk, S. Shen, L. Guo, and S. Mathur: Constructing Fe_2O_3/TiO_2 core–shell photoelectrodes for efficient photoelectrochemical water splitting. *Nanoscale* **7**, 10094 (2015).
25. A. Mettenbörger, Y. Gönüllü, T. Fischer, T. Heisig, A. Sasinska, C. Maccato, G. Carraro, C. Sada, D. Barreca, L. Mayrhofer, M. Moseler, A. Held, and S. Mathur: Interfacial insight in multijunction metal oxide photoanodes for water-splitting applications. *Nano Energy* **19**, 415 (2016).
26. L. Badia-Bou, E. Mas-Marza, P. Rodenas, E.M. Barea, F. Fabregat-Santiago, S. Gimenez, E. Peris, and J. Bisquert: Water oxidation at hematite photoelectrodes with an iridium-based catalyst. *J. Phys. Chem. C* **117**, 3826 (2013).
27. F. Le Formal, M. Grätzel, and K. Sivula: Controlling photoactivity in ultrathin hematite films for solar water-splitting. *Adv. Funct. Mater.* **20**, 1099 (2010).
28. K. Sivula, F. Le Formal, and M. Grätzel: Solar water splitting: Progress using hematite (α-Fe_2O_3) photoelectrodes. *ChemSusChem* **4**, 432 (2011).
29. O. Zandi and T.W. Hamann: The potential versus current state of water splitting with hematite. *Phys. Chem. Chem. Phys.* **17**, 22485 (2015).

https://doi.org/10.1557/jmr.2017.465 Published online by Cambridge University Press

30. A.G. Tamirat, W-N. Su, A.A. Dubale, H-M. Chen, and B-J. Hwang: Photoelectrochemical water splitting at low applied potential using a NiOOH coated codoped (Sn, Zr) α-Fe_2O_3 photoanode. *J. Mater. Chem. A* **3**, 5949 (2015).
31. B. Iandolo, B. Wickman, I. Zoric, and A. Hellman: The rise of hematite: Origin and strategies to reduce the high onset potential for the oxygen evolution reaction. *J. Mater. Chem. A* **3**, 16896 (2015).
32. A.P. Grosvenor, B.A. Kobe, M.C. Biesinger, and N.S. McIntyre: Investigation of multiplet splitting of Fe 2*p* XPS spectra and bonding in iron compounds. *Surf. Interface Anal.* **36**, 1564 (2004).
33. T. Yamashita and P. Hayes: Analysis of XPS spectra of Fe^{2+} and Fe^{3+} ions in oxide materials. *Appl. Surf. Sci.* **254**, 2441 (2008).
34. C. Zhu, C. Li, M. Zheng, and J-J. Delaunay: Plasma-induced oxygen vacancies in ultrathin hematite nanoflakes promoting photoelectrochemical water oxidation. *ACS Appl. Mater. Interfaces* **7**, 22355 (2015).
35. K. Wandelt: Photoemission studies of adsorbed oxygen and oxide layers. *Surf. Sci. Rep.* **2**, 1 (1982).
36. Y. Hu, F. Boudoire, I. Hermann-Geppert, P. Bogdanoff, G. Tsekouras, B.S. Mun, G. Fortunato, M. Graetzel, and A. Braun: Molecular origin and electrochemical influence of capacitive surface states on iron oxide photoanodes. *J. Phys. Chem. C* **120**, 3250 (2016).
37. X. Zhang, P. Klaver, R. van Santen, M.C.M. van de Sanden, and A. Bieberle-Hütter: Oxygen evolution at hematite surfaces: The impact of structure and oxygen vacancies on lowering the overpotential. *J. Phys. Chem. C* **120**, 18201 (2016).
38. D.K. Bora, A. Braun, S. Erat, R. Löhnert, A.K. Ariffin, R. Manzke, K. Sivula, T. Graule, M. Grätzel, and E.C. Constable: Evolution of an oxygen near-edge X-ray absorption fine structure transition in the upper hubbard band in α-Fe_2O_3 upon electrochemical oxidation. *J. Phys. Chem. C* **115**, 5619 (2011).
39. M. Forster, R.J. Potter, Y. Ling, Y. Yang, D.R. Klug, Y. Li, and A.J. Cowan: Oxygen deficient α-Fe_2O_3 photoelectrodes: A balance between enhanced electrical properties and trap-mediated losses. *Chem. Sci.* **6**, 4009 (2015).
40. C.H.M. van Oversteeg, H.Q. Doan, F.M.F. de Groot, and T. Cuk: In situ X-ray absorption spectroscopy of transition metal based water oxidation catalysts. *Chem. Soc. Rev.* **46**, 102 (2017).
41. S. Shen, J. Zhou, C.L. Dong, Y. Hu, E.N. Tseng, P. Guo, L. Guo, and S.S. Mao: Surface engineered doping of hematite nanorod arrays for improved photoelectrochemical water splitting. *Sci. Rep.* **4**, 6627 (2014).
42. J. Suntivich, W.T. Hong, Y-L. Lee, J.M. Rondinelli, W. Yang, J.B. Goodenough, B. Dabrowski, J.W. Freeland, and Y. Shao-Horn: Estimating hybridization of transition metal and oxygen states in perovskites from O K-edge X-ray absorption spectroscopy. *J. Phys. Chem. C* **118**, 1856 (2014).
43. Y. Fu, C-L. Dong, Z. Zhou, W-Y. Lee, J. Chen, P. Guo, L. Zhao, and S. Shen: Solution growth of Ta-doped hematite nanorods for efficient photoelectrochemical water splitting: A tradeoff between electronic structure and nanostructure evolution. *Phys. Chem. Chem. Phys.* **18**, 3846 (2016).
44. J.P. Crocombette, M. Pollak, F. Jollet, N. Thromat, and M. Gautier-Soyer: X-ray-absorption spectroscopy at the Fe $L_{2,3}$ threshold in iron oxides. *Phys. Rev. B* **52**, 3143 (1995).
45. G.v.d. Laan and I.W. Kirkman: The 2*p* absorption spectra of 3*d* transition metal compounds in tetrahedral and octahedral symmetry. *J. Phys.: Condens. Matter* **4**, 4189 (1992).
46. F. Jiménez-Villacorta, C. Prieto, Y. Huttel, N.D. Telling, and G. van der Laan: X-ray magnetic circular dichroism study of the blocking process in nanostructured iron–iron oxide core–shell systems. *Phys. Rev. B* **84**, 172404 (2011).
47. M. Pollak, M. Gautier, N. Thromat, S. Gota, W.C. Mackrodt, and V.R. Saunders: An in situ study of the surface phase transitions of α-Fe_2O_3 by X-ray absorption spectroscopy at the oxygen K edge. *Nucl. Instrum. Meth. B* **97**, 383 (1995).
48. T-P. Ruoko, K. Kaunisto, M. Bärtsch, J. Pohjola, A. Hiltunen, M. Niederberger, N.V. Tkachenko, and H. Lemmetyinen: Sub-picosecond to second time-scale charge carrier kinetics in hematite–titania nanocomposite photoanodes. *J. Phys. Chem. Lett.* **6**, 2859 (2015).
49. M. Barroso, S.R. Pendlebury, A.J. Cowan, and J.R. Durrant: Charge carrier trapping, recombination and transfer in hematite (α-Fe_2O_3) water splitting photoanodes. *Chem. Sci.* **4**, 2724 (2013).
50. S.R. Pendlebury, X. Wang, F. Le Formal, M. Cornuz, A. Kafizas, S.D. Tilley, M. Gratzel, and J.R. Durrant: Ultrafast charge carrier recombination and trapping in hematite photoanodes under applied bias. *J. Am. Chem. Soc.* **136**, 9854 (2014).
51. S.R. Pendlebury, A.J. Cowan, M. Barroso, K. Sivula, J. Ye, M. Gratzel, D.R. Klug, J. Tang, and J.R. Durrant: Correlating long-lived photogenerated hole populations with photocurrent densities in hematite water oxidation photoanodes. *Energy Environ. Sci.* **5**, 6304 (2012).
52. S. Khan, G. Azimi, B. Yildiz, and K.K. Varanasi: Role of surface oxygen-to-metal ratio on the wettability of rare-earth oxides. *Appl. Phys. Lett.* **106**, 061601 (2015).
53. Z. Li, Y. Wang, A. Kozbial, G. Shenoy, F. Zhou, R. McGinley, P. Ireland, B. Morganstein, A. Kunkel, S.P. Surwade, L. Li, and H. Liu: Effect of airborne contaminants on the wettability of supported graphene and graphite. *Nat. Mater.* **12**, 925 (2013).

Supplementary Material

To view supplementary material for this article, please visit https://doi.org/10.1557/jmr.2017.465.

https://doi.org/10.1557/jmr.2017.465 Published online by Cambridge University Press